76th International Astronautical Congress (IAC 2025), Sydney, Australia, 29 Sep-3 Oct 2025.

IAC-25,B1,3,3,x100682

Characterization of the next generation of ultra-wideband uncooled microbolometer arrays at INO

Christian Proulx [a]*, Francis Généreux [a], Jean-François Lavigne [a], Antoine Létourneau [a], Hélène Spisser [a], Martin Grenier [a], Bruno Fisette [a], Michel Poirier [a], Michael Buchen [a]

[a] Institut National d'Optique, 2740 Rue Einstein, Québec, Québec, Canada, G1P 4S4
* Corresponding Author

Abstract

INO's microbolometers with gold black coating are renowned for their exceptional sensitivity across a broad waveband ranging from the UV to the far infrared. The ultra-wideband sensitivity enables a wide array of cutting-edge applications in Earth observation and planetary exploration. For example, these detectors play a crucial role in measuring the Earth's radiative budget, as exemplified by their integration into the EarthCARE mission's Broadband Radiometer (BBR), where they provide precise observations of energy exchange between the planet and space. In planetary science, the Lunar Thermal Mapper relies on these microbolometers to conduct highly accurate cold temperature measurements, essential to calibrate HVM^3 measurements for water detection and for understanding the Moon's surface composition and thermal behavior. They can also be used for the detection and the characterization of thin ice clouds, advancing our understanding of their role in climate regulation and atmospheric dynamics.

This paper presents the recent development at INO of its next generation ultra-wideband uncooled microbolometer arrays. These arrays are based on native 512x384 pixel sensors with a 28 µm pitch. A gold black layer is deposited on the array and can be trimmed with different pixel formats depending on the spatial resolution and spectral responsivity required for the targeted application.

We report on both simulated and measured key performance metrics, including noise equivalent power (NEP), time constant, spectral responsivity, and long-term measurement stability. Notably, the ROIC demonstrates low correlated noise, reducing the need for additional noise mitigation strategies. The spectral response is uniform across the tested band, with a slight reduction above 30 µm, which is currently under investigation.

Finally, we present qualification tests and results for the space environment. The packaged FPAs successfully passed rigorous vibration, shock, thermal cycling, and total ionizing dose radiation tests, confirming their robustness for demanding space applications.

Keywords: Microbolometers, far infrared, uncooled, radiometry

Acronyms/Abbreviations

ADC	Analog-to-Digital Converter
AOS	Atmospheric Observing System
BBR	Broadband Radiometer
CMOS	Complementary Metal-Oxide-Semiconductor
CSA	Canadian Space Agency
CTE	Coefficient of Thermal Expansion
FIR	Far InfraRed
FIRR	Far Infrared Radiometer
FOM	Figure of Merit
FOV	Field-of-View
FPGA	Field-Programmable Gate Array
FPA	Focal Plane Array
GIFOV	Ground-Projected Instantaneous Field-of-View
HDISCC	High-Definition Infrared Space Camera Core
INO	Institut National d'Optique
IR	Infrared
LTM	Lunar Thermal Mapper
MIDAS	Miniaturized Infrared Detector of Atmospheric Species
MTF	Modulation Transfer Function
NEI	Noise Equivalent Irradiance
NEP	Noise Equivalent Power
NER	Noise Equivalent Radiance
ROIC	Read Out Integrated Circuit
SRS	Shock Response Spectrum
TCR	Temperature Coefficient of Resistance
TEC	Thermoelectric Cooler
THz	Terahertz
TICFIRE	Thin Ice Clouds in the Far InfraRed Emission
TID	Total Ionising Dose
UV	Ultraviolet

1. Introduction

INO has been involved in the development of uncooled bolometer detectors for over 30 years, with devices addressing needs spanning from the UV to the THz spectral regions. Wide broadband applications and those focusing on far infrared and THz regions of the spectrum rely on the use of gold black as the absorber of the incoming signal. Gold black deposition and micromaching processes were originally developed in the

context of the development of the EarthCARE Broadband Radiometer (BBR) detectors [9][10], which was recently launched [14]. Detectors of various formats and pitches have been developed over the years with the more recent being IRM384-based detectors with a format of 384x288 pixels on a 35-µm pitch. Such detectors have been considered in space mission studies, used in some spaceborne instruments, and also in the context of prototype development to support prospective missions.

The IRM384 detector is used for the Lunar Thermal Mapper (LTM) instrument developed by the University of Oxford for the Lunar TrailBlazer mission[1][3], a multispectral radiometer covering the spectral range from 7 µm to 100 µm. Another use of the detector is in the Trutinor breadboard led by the NASA Langley Research Center, which consists in a concept study for the next-generation of Earth radiation budget instrumentation [13]. The detector was also integrated in the Miniaturized Infrared Detector of Atmospheric Species (MIDAS) developed at the University of Hawaii for spectrally sensing high-temperature phenomena in the 3-6 µm range [8]. The Primitive Object Volatile Explorer (PrOVE) mission concept [2] also considered its use for the study of surface structure and volatile inventory of comets in the mid-wave infrared.

In recent years, INO has been developing a new FPA platform, namely the IRM1024 FPA, which implements a format of 512x384 pixels on a 28-µm pitch for broadband and far-IR applications. This new detector is now being considered for the Thin Ice Clouds in the Far Infrared Emission (TICFIRE) instrument, which is a planned CSA contribution to the NASA Atmospheric Observing System (AOS) constellation of spacecrafts.

In this paper we present results associated to this development, including a description of the FPA and detector assembly, as well as characterization results for functional, performance and environmental tests. Some of this work was realized in a CSA-funded development project associated to the prospective TICFIRE instrument.

2. Device description

The detector developed includes an INO IRM1024 FPA within a rugged metallic detector assembly. This section describes both aspects in detail.

2.1 Focal plan array (FPA)

The IRM1024 FPA was recently developed at INO to replace the legacy IRM384. The IRM1024 offers a few improvements over the IRM384 detector platform. The IRM1024 allows for a better overall sensitivity performance since it implements a higher active pixel bias voltage than the IRM384, which promotes a greater input-referred response. The CMOS and reference pixel noise are also negligible, which makes IRM1024 noise dominated by the active bolometers. The IRM1024 provides for a greater pixel-level dynamic range; this allows a greater level of optimization of the operating parameters, especially in the case of the detector being used in instruments with faster optics, higher transmittance and wider spectral channels. A global "TCR-matching" function is available in the IRM1024 detector to better immunize the average output offset against operating temperature drifts, translating into better radiometric stability when used in radiometer instruments. The IRM1024 finally features a gain compensation which make the FPA response mainly insensitive with respect to a temperature change, once again promoting radiometric stability at the instrument level in addition to a lower TEC power consumption.

For pixels targeting the far-infrared spectral region, INO has developed native pixels of 28-µm pitch, which translate into a format of 512x384 for a focal plane area of 14.3 mm by 10.8 mm (compared to 13.4 mm by 10.2 mm for the IRM384). Two pixel variants exist: a fast version, with a thermal time constant around 17 ms, and a slower version with increased responsivity [7]. The results presented in section 3 will focus on the slower more responsive pixel variant.

Absorption in the wide spectral region spanning from the UV to the FIR is ensured by the use of a gold black coating, which is processed internally at INO [9]. The coating is deposited on top of the active bolometers and processed at the die level. Once deposited, it is possible to trim the gold black by a laser micromachining process [6]. This was achieved at various pitches that correspond to an integer multiple of the native pixel pitch of 28 µm. At the narrower end, pixels have been trimmed at the same pitch than the native pitch [7], but also at wider pitches including 56 µm, 84 µm, 112 µm and 140 µm. The gold black trimming is paramount to maintain a high detector MTF. At greater wavelengths however, because of the diffraction limit associated to the telescope being eventually used at the instrument level, it may be unnecessary to use very narrow trimming pitches. A risk is associated with using narrower pitches as the gold black trimming grid comes down to dimensions that approaches wavelengths of interest in the system. For example, a narrow trimming pitch may optimize performance at shorter wavelengths but reduce detector absorption at longer wavelengths. Additionally, spatial resolution does not necessarily scale proportionally with trimming pitch. The results of section 3 will focus on detector pixels with gold black trimmed at the 140 µm pitch, which consists in a low-risk approach for wide band radiometry extending to 75 µm and above. Other trimming pitches could however be characterized to better establish the performance across different wavelengths and pitch values. A characterization facility was recently developed at INO to measure the MTF of detectors and gold-blackened pixels will be characterized in the near future.

The trimming process was indeed developed to support the various trimming pitches and FPA format. For example, the trimming dose was optimized to insure full trimming of gold black for every individual pixel within the FPA with an accuracy better than ± 2.5 µm and a trimming width smaller than 6 µm. The dose value was also set to account for the gold black thickness variation within the array, from die to die and from lot to lot. The gold black thickness variation from lot to lot, as measured on witness samples coated alongside the FPAs, is less than ± 5.4% peak-to-peak. Impact of this thickness variation on the specular reflectance was found to be negligible as depicted in Fig. 1.

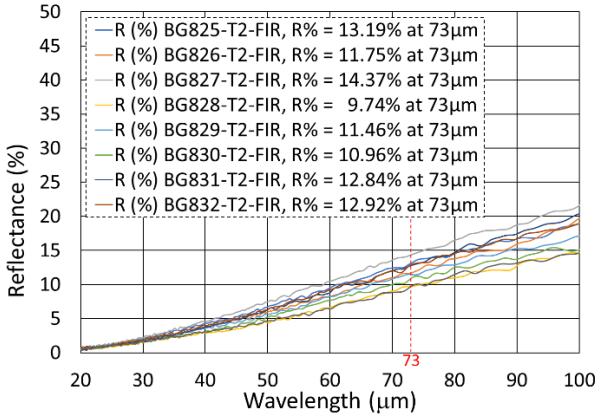

Fig. 1. FIR reflectance of Gold Black deposition lots

The noise equivalent power (NEP) of a 28-µm pitch microbolometer ranges between 6.5 pW and 7.5 pW. After binning, the noise level decreases from 13 to 4 counts, resulting in a NEP between 55 pW and 65 pW. By comparison, the NEP of a 35-µm pitch microbolometer in the IRM384 detector is 26 pW according to [5]. After binning, this pixel achieves an effective pitch of 140 µm, with noise reduced from 20 to 10 counts, which leads to a NEP of 208 pW. Thus, for a microbolometer with a 140-µm pitch, the IRM1024 provides a factor of 3 improvement in NEP compared to the IRM384. Even when accounting for the higher frame rate of the IRM384 (50 Hz compared to 30 Hz for the IRM1024), which provides greater temporal averaging capability, the NEP improvement remains greater than a factor of 2. Additionally, both detectors exhibit a similar time constant (27 ms), which implies that the improvement in the figure of merit (FOM), here defined as the product of the NEP and the time constant, is preserved accordingly.

It is noteworthy that this increase in sensitivity, or improvement in FOM, is observed across a wide range of trimming pitches, as illustrated in Fig. 2. For this analysis, the sensitivity is defined as the noise equivalent irradiance (NEI), which we define as the ratio of the NEP over the pixel pitch (Λ) squared, and which is directly related to the instrument-level noise equivalent radiance (NER) according to the following expression:

$$NER = \frac{4F^2}{\pi\tau_o} \cdot \frac{NEP}{\Lambda^2} = \frac{4F^2}{\pi\tau_o} \cdot NEI \qquad (1)$$

where F denotes the F-number and τ_o the transmittance of the optical system. This plot highlights the potential of the IRM1024 to improve performance by a factor ranging from 2.5 to 3.5 compared to the IRM384, depending on the selected trimming pitch. Furthermore, it demonstrates that for a given F-number and ground-projected instantaneous field-of-view (GIFOV), it is advantageous to consider larger trimming pitches, provided that the FPA format can accommodate the intended field of view and that a longer focal length is acceptable.

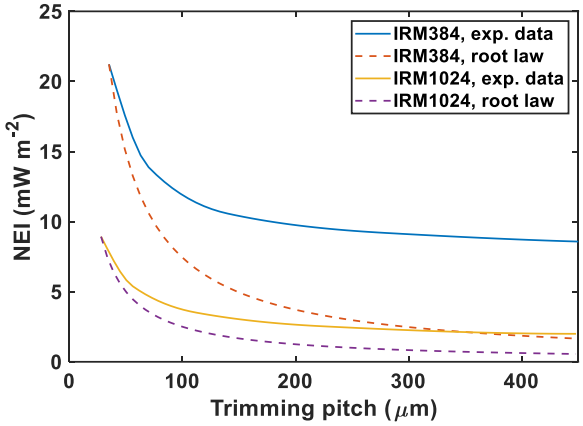

Fig. 2. NEI as a function of the trimming pitch.

Radiometric applications related to the far infrared often rely on data in the mid to thermal infrared. Over such a wide spectral range, using a reflective telescope is a common choice, with implications on the achievable field-of-view (FOV). Because of the limited FOVs typically associated with reflective telescopes, only a partial subset of the FPA pixels will be illuminated. This partial use of the FPA allows non-illuminated pixels to be incorporated into signal correction algorithms, potentially reducing detector noise, when averaging is applied (e.g., via spatial binning of pixels), to a level approaching the theoretical limit set by the square root law (see dashed lines in Fig. 2). The detector developed by INO exhibits such a feature and deliver an extinction ratio appropriate for this type of signal correction. In a recent study, INO determined that extinction ratios in the order of 10,000:1 can be necessary to allow for such corrections to be efficient without adding additional artefacts or involving noise removal by post-processing. The extinction ratio depends on the ratio of the scene dynamic range over the sensitivity (e.g. noise-equivalent radiance) required by the application.

At the FPA level, two areas are defined: a central area with active pixels and a peripheral area with pixels of

lower responsivity. Achieving truly blind pixels with a 10,000:1 extinction ratio cannot be achieved by the pixels of the peripheral area alone and thus needs to be coupled with other means of signal extinction as discussed in the next section. In a recent development project for the CSA, INO produced prototype FPAs that had a central area of 240x240 native pixels (28-µm pitch) with the rest of the array (peripheral area) being used with less responsive pixels. Two less-responsive pixel variants were tested to provide for extinction ratios of about 25:1 and 40:1.

2.2 Detector assembly

The detector assembly used for the environmental characterization discussed in section 3 is the INO Gen5a. This detector platform consists in a rugged metallic package designed to provide the necessary robustness typically associated with space mission environments (temperature, vibrations and shocks) [4]. This platform was developed to be flexible: it can accommodate different detector FPAs and optical filter(s) inside the detector cavity very close to the FPA [7]. The assembly also includes a thermoelectric cooler (TEC), a thermistor and a routing circuit, as well as a pressure gauge and electrically reactivable getters. With an appropriate optical window, the assembly can be used under dynamic pumping conditions or be vacuum-sealed.

The detector assembly was recently adapted to specific needs in a development project with the CSA. With the intention to use the detector over a wide spectral range (from 4 µm to > 73 µm), a diamond window is used. The window dimensions are adapted from previous designs and made larger to accommodate a central area of 240x240 native pixels. The detector assembly is vacuum sealed because of the prospect of being used in an airborne mission.

A few environmental requirements were evaluated to be riskier with respect to the detector assembly design. The more stringent environments require survival at temperatures down to -55 °C and resistance to shock response spectra (SRS) up to 1020 g over the 100 Hz to 10 kHz frequency range. The risks identified were associated to the integrity of the die attach, window solder (which can affect vacuum integrity), TEC and TEC attach. A combination of finite-element analyses and preliminary tests on partial prototype assemblies was used to assess and adapt the design. With limited information on the properties of the bonding materials and considering the limitations of FEA software, the risks related to the detector assembly could not be fully mitigated prior to the environmental test campaign. This prompted the monitoring of functional parameters to validate the integrity of the interfaces at risk. A description of the functional parameters monitored and the means to measured them are provided in section 3.2.

Another aspect of adaptation of the detector assembly that was considered in the development project is the implementation of an optomechanical mask to shield the less-responsive pixels, located in the peripheral area of the FPA, from the incoming signal. The Gen5a detector assembly has already been implemented with butcher-block filter arrays as close as 500 µm of the FPA [7]. Since no such filter implementation is of interest in the project, it was a relatively straightforward modification to include the optomechanical mask in place of the filter assembly. The part designed is made of tungsten-copper alloy, which combines a good CTE match with the routing circuit while providing adequate thermal properties to efficiently diffuse the absorbed heat and avoid the self-heating of the mask. The mask is further blackened with the Acktar Ultra Black coating to minimize stray light. A non-sequential ray-tracing analysis was conducted and demonstrated that the mask had the ability to provide for an extinction ratio better than 1000:1 for most of the pixels of the peripheral area, and as high as 10,000:1 in the outer most region of the peripheral area (see Fig. 3).

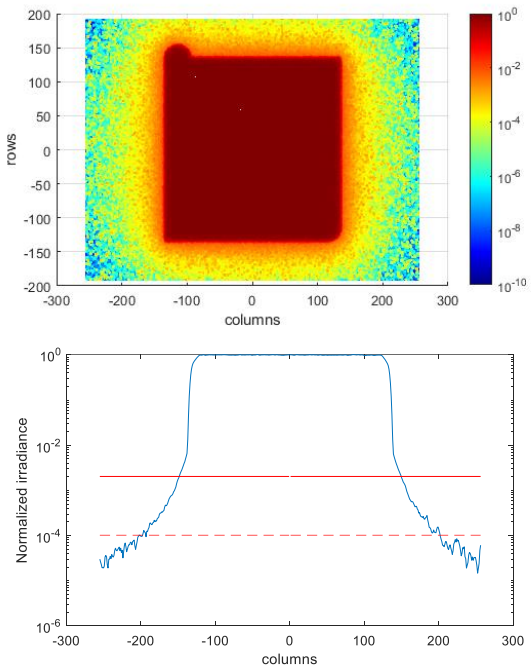

Fig. 3. Extinction ratio for pixels in the peripheral area

Because of the uncertainty associated to the ray-tracing analysis, namely the material surface properties, and because signal correction algorithms are more efficient when a larger number of pixels can be used, the better way to achieve the targeted 10,000:1 extinction ratio is deemed to combine the optomechanical mask with less responsive pixels in the peripheral area. However, in the development project, the implementation of these features was abandoned because the risks introduced by the optomechanical mask, primarily concerns regarding the integrity of the mask

attachment and the presence of additional outgassing sources within the detector cavity, were deemed to outweigh the performance benefits offered by the signal correction for the specific use cases. Furthermore, the performance requirements of the development project could be met without resorting to such noise-compensation strategies. Experimental validation of these features could be explored in a future project.

3. Results and discussion

A test campaign was conducted on four detector devices such as those described in the previous section. One of these assemblies is shown in Fig. 4.

Fig. 4. Detector assembly s/n 2024-0008

The detector assemblies were tested for functionality, performance, and environmentally in order to determine their ability to be qualified in the context of their eventual use in airborne and orbital missions.

Two detectors were tested in a flight-like qualification test campaign, including random vibrations, shocks, temperature cycling, and total ionising dose (TID) radiation exposure. The test sequence for these two detectors is shown in Fig. 5. The order of testing was set as a worst-case scenario with the temperature cycling conducted before the random vibration and shock tests, as the low-temperature survival condition is known to induce the higher level of stress at critical interfaces. TID radiation tests were introduced right after temperature cycling due to schedule constraints from the availability of associated sub-contractors.

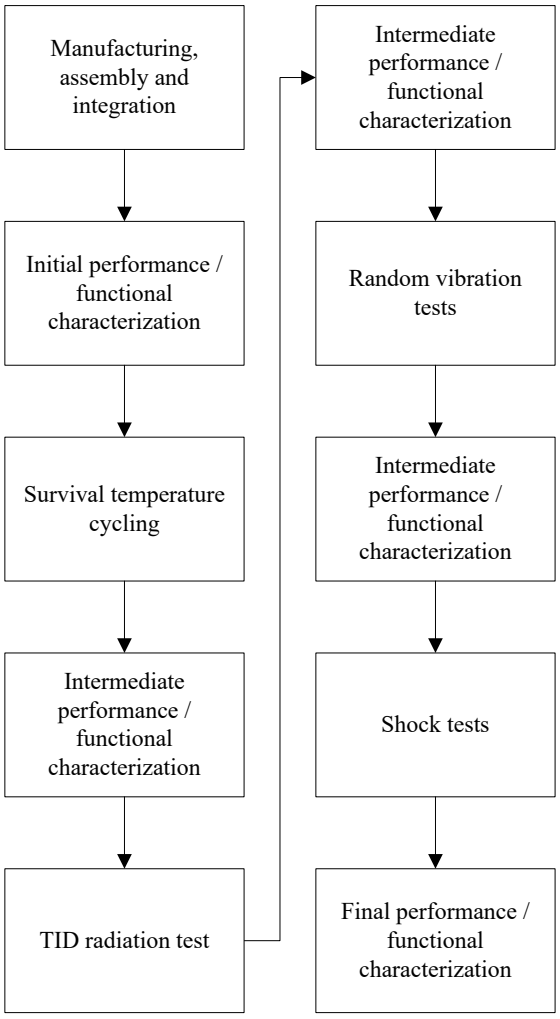

Fig. 5. Flight-like qualification test sequence

The other two units, which are expected to be used in an eventual airborne campaign, were submitted to a more straightforward test sequence that includes only an operational vibration test in addition to the functional and performance characterization (see Fig. 6).

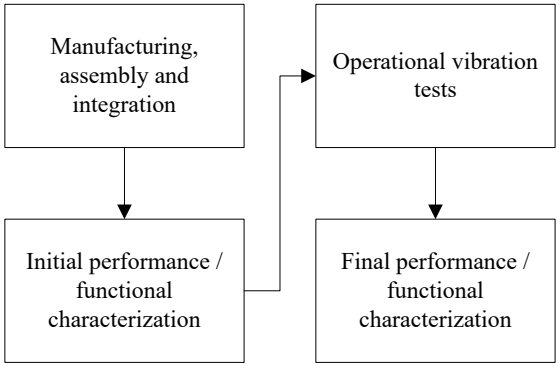

Fig. 6. Operational vibration test sequence

To conduct the functional and performance tests, the detectors need to be connected to an ITP1024 test jig, which provides the necessary commercial-grade proximity and control electronics to operate the IRM1024 detector packaged in a Gen5a assembly (see Fig. 7). The ITP1024 includes the functionality of providing the supply voltages and the low-noise bias voltages for the FPA. It further provides for the (16-bit) analog-to-digital conversion of the FPA output signal, and for sending the digital data packets to a PC via a USB connection. The ITP1024 includes an FPGA and microcontroller to generate the appropriate FPA timings, set the ROIC registers for the operating parameters, control the ADC, and implement the control for the package thermoelectric cooler that sets the FPA operating temperature. The ITP1024 was designed and validated so that its contribution to the performance when used with an IRM1024 detector is close to negligible. The detector is also compatible with the INO high-definition infrared space camera core (HDISCC) electronics recently developed in the context of a commercial constellation mission [7]. The detector performance measured when used with an ITP1024 is representative of that expected in a HDISCC assembly.

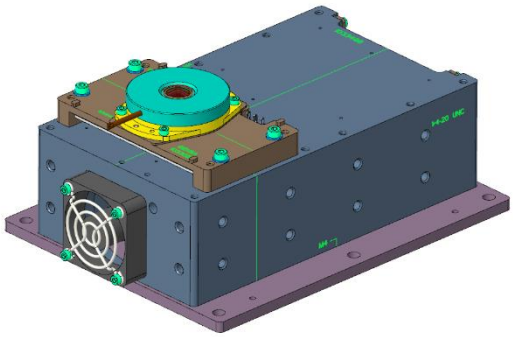

Fig. 7. Detector with ITP1024 electronics test jig

3.1 Survival environmental tests

The survival environmental tests were conducted on unbiased detectors with the assemblies mounted on jigs to interface them with the appropriate test equipment.

For the temperature cycling, the detector units were mounted on a test base plate and put in a non-condensing environmental chamber operated at ambient pressure. The temperature was monitored with calibrated thermocouples attached to the test base plate with tape. The two detectors were tested simultaneously and exposed to 10 cycles between +60°C and -55°C.

For the TID radiation test, one of the units was tested with a proton source at Triumf facilities in Vancouver (British Columbia) while the other was tested with a gamma-ray source at Nordion facilities in Ottawa (Ontario). The test at Triumf was conducted in their BL2C facilities with 105-MeV energy protons to a total dose of 10.0 krad(Si). The unit tested at Nordion was irradiated after a dose mapping exercise in a chamber equipped with Co-60 sources to a total dose evaluated between 11.1 krad and 12.9 krad.

The random vibration tests were performed with the detectors mounted in a protective tooling validated to be stiff enough not to impact the vibration levels seen by the detector unit under test. The test was performed on INO's in-house shaker with miniature tri-axial accelerometers used to control and monitor the vibrations on the tooling and shaker interface. The test profile consisted in the qualification profile from GSFC-STD-7000B, which totals 14.1 Grms, for two minutes in each axis. A low-level sine sweep of 0.1 g at frequencies from 20 Hz to 2000 Hz (2 octaves/minute) was performed before and after imposing the random vibration profile. No significant changes were noted between the sine sweeps. The target level of 14.1 Grms for random vibrations was reached for each detector in all three axes, with the control value remaining below ± 1% of the target.

The SRS shock test was conducted at MGA Research Corporation, with the detectors mounted in a protective tooling as for the random vibration tests. The targeted profile and envelope are shown in Fig. 8. The two detectors were tested after setup calibration and risk-mitigation preliminary tests. Functional and partial performance tests were further conducted on-site at MGA between axis to help identify when any degradation would have taken place. In the end, the two tested detectors did not show any significant degradation in their physical integrity or in performance, as discussed below.

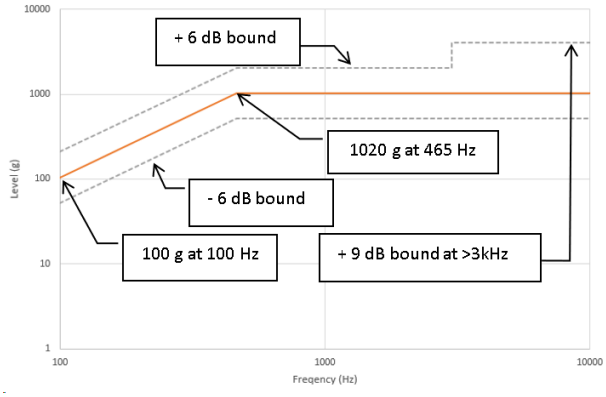

Fig. 8. SRS level requirement

3.2 Functional tests

The functional tests results presented in this section focus on the validation of the integrity of critical interfaces in the design of the detector assembly.

The integrity of the window solder joint was verified by monitoring the residual pressure inside the detector assemblies. The pressure was evaluated to be less than 2.5 mTorr throughout the environmental tests, without

any significant increase noted at any measurement. The evaluation is based on a combination of direct pressure gauge measurement on some units and monitoring of the pixels responsivity on others since some pressure gauges were damaged during the manufacturing, assembly and integration process.

The integrity of the FPA die-attach was monitored via a measurement of the temperature difference between the FPA and the control thermistor fixed on the routing circuit. The temperature of the FPA is measured via a diode within the IRM1024 chip. The temperature of the FPA is slightly increased with respect to the routing circuit due to heat dissipation within the CMOS electronics. The measured temperature difference did not vary by more than 0.1°C, which is indicative of the stability of the interface in INO experience with such detectors. An important failure of the FPA attach, even partial, typically results in an increase of the temperature difference greater than 2-3°C.

The integrity of the TEC and TEC-attach interfaces were validated by measuring the TEC AC resistance (using an LCR meter), and its thermal time constant and figure of merit (using the Harman method with a function generator and an oscilloscope). A variation by more than ± 5% in any of the three parameters can be associated to a TEC or TEC-attach defect [12]. The variation between two consecutive measurements before and after an environmental test was always less than 2%, well within the failure criteria mentioned above.

3.3 Noise-equivalent power (NEP) tests

Noise-equivalent power (NEP) has been measured for the four detectors having undergone both types of environmental testing. Detectors 2024-0008 and 2024-0009 have been subjected to the flight-like qualification sequence described in Fig. 5 and detectors 2024-0011 and 2024-0012 to the operational vibration test sequence described in Fig. 6. Measurements have been conducted before and after each environmental testing round. The setup used here allows a NEP-measurement in the 8-12 µm band on the whole FPA. Specifically, we consider here the central region of 48 x 48 pixels with a 140 µm pitch as defined by gold black trimming. Each 140-µm pixel corresponds to a 5x5 bin of native pixels with a 28-µm pitch.

The NEP test setup consists in a large area black body and an F/1 equivalent temperature-controlled baffle. Detectors are installed in an ITP1024 test jig for this measurement (c.f. Fig. 7). An 8-12 µm filter is placed in front of the detector. An in-house software controls the shutter, the blackbody temperature and the camera acquisition, allowing automated measurements. A diagram of this setup is presented Fig. 9.

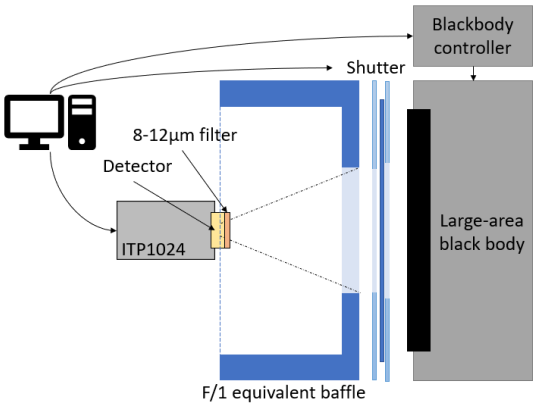

Fig. 9. Layout of the NEP test setup

NEP results for detectors through the environmental test sequence are presented in Fig. 11. No significative change in NEP median value or dispersion is to be noted through the environmental test campaign. The same observation applies for both detectors having undergone operational vibrations (Fig. 12).

3.4 Thermal time constant tests

The temporal response of the detector pixels is described by an exponential curve characterized by a time constant τ. To measure this parameter, the detector is placed in front of a blackbody. Infrared radiation on the detector is modulated by a fast shutter; a diaphragm is used to reduce the visible area of the shutter and thus the transition time between full illumination and dark scene (see Fig. 10). The slope determined by a linear fit on the logarithm of the decreasing detector signal gives then $-1/\tau$.

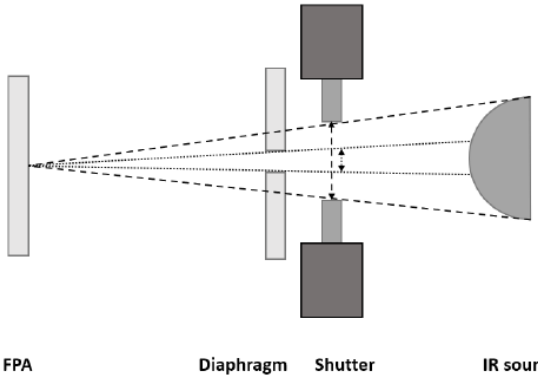

Fig. 10. Layout of the time constant measurement setup

Time constant results for detectors through the environmental test sequence are presented in Fig. 13. No significative change in the time constant median value or dispersion is to be noted through the environmental test campaign. The same observation applies for both detectors having undergone operational vibrations (Fig. 14)

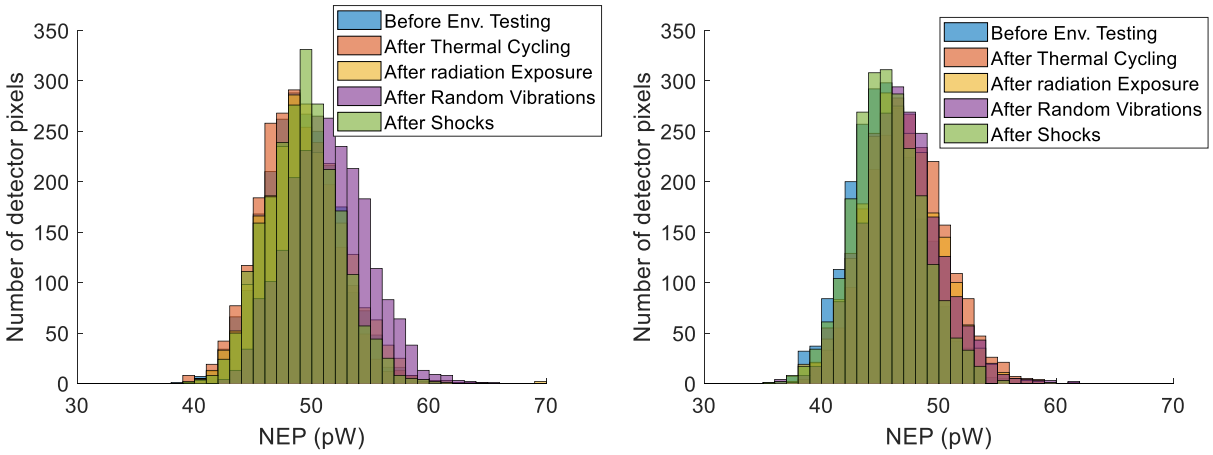

Fig. 11. NEP histograms measured for detector 2024-0008 (left) and detector 2024-0009 (right) through environmental testing

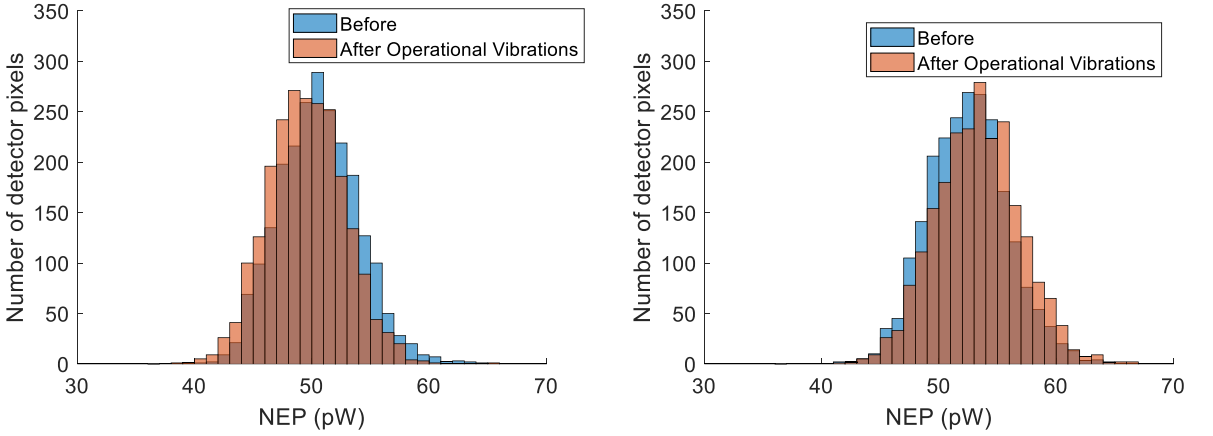

Fig. 12. NEP histograms measured for detector 2024-0011 (left) and detector 2024-0012 (right) before and after operational vibrations

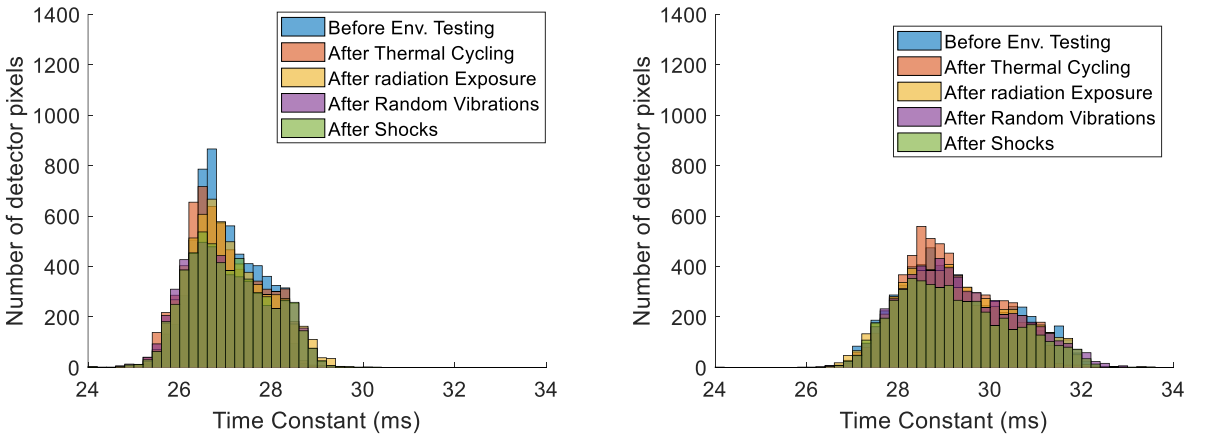

Fig. 13. Time constant histograms measured for detector 2024-0008 (left) and detector 2024-0009 (right) through environmental testing

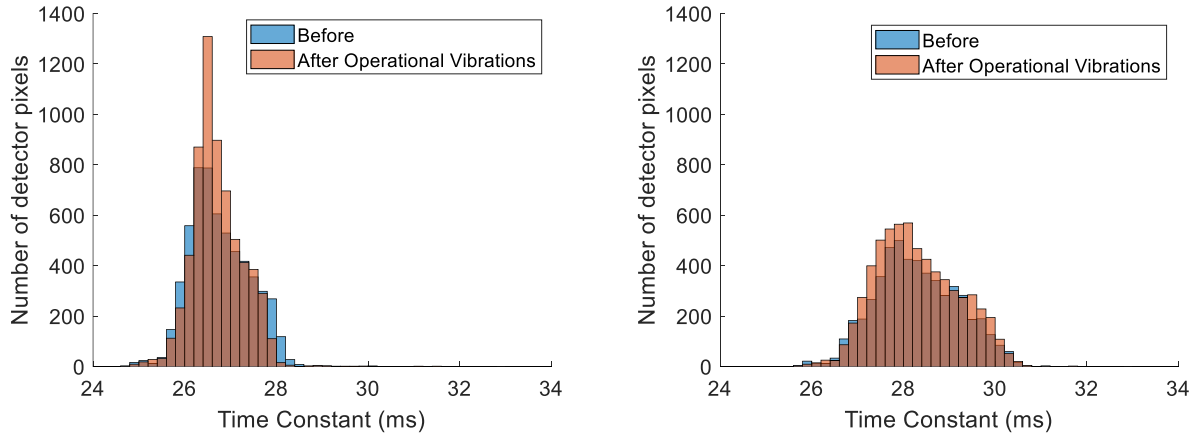

Fig. 14. Time constant histograms measured for detector 2024-0011 (left) and detector 2024-0012 (right) before and after operational vibrations

3.5 Spectral responsivity characterization

The responsivity of the four detectors having undergone environmental testing has been measured in nine spectral channels using passband filters between 8 µm and 50 µm before and after environmental testing. An additional measurement with a long-wave pass filter of 33 µm cut-on wavelength has been carried out at the end of the environmental test sequence. A detailed description of the FIRR instrument used for these measurements can be found in [11].

The results are shown in Fig. 17 for detector 2024-0009 with similar results obtained for the other three detectors. In the figure, the length of the bar corresponds to the nominal spectral channel defined by the filter used for measurement. The responsivity is the averaged value over the pixels illuminated by the telescope of the FIRR instrument, covering typically an area of 90 detector pixels (140-µm pitch). There is no significant responsivity degradation throughout the test campaign.

The responsivity is very uniform over the subranges of 8-14 µm and 17-23 µm. In general, the responsivity decreases at longer wavelengths, most notably in the 22-28 µm and 30-50 µm bands. This is likely due to the lower absorbance of the gold black coating in these bands (c.f. Fig. 1 and [9]). The loss of responsivity is however greater than the corresponding increase of reflectance measured during the production of the gold black. One aspect to consider is the fact that the reflectance measurements are limited to specular reflectance characterization whereas the gold black could have a diffuse component of reflectance. The specular / diffuse reflectance of the coating characteristics may also vary with wavelength, as is typical of coatings characteristics extending in the far infrared. Other reasons to explain the difference may be linked with the FIRR instrument used for responsivity measurements, for example wavelength-dependent stray light may affect the responsivity measurements differently in the various spectral channels investigated. The spectral emissivity of the blackbodies used for measurement could also influence the results differently in the various bands.

3.6 Operational vibration tests

The detectors were tested individually for operational vibrations with the ITP1024 assembly (c.f. Fig. 7) mounted on an interface fixture to the INO in-house shaker. Miniature tri-axial accelerometers are used to control and monitor vibrations on the tooling and shaker interface jig, and to monitor cross-axis accelerations. A 4-in large area blackbody was brought in the field of view of the detector with a manual forklift. The blackbody is brought in close proximity to the detector while avoiding any risks of contact between the detector and the blackbody. The z-axis configuration is shown in Fig. 15 but the ITP1024 assembly was tested in all three axes.

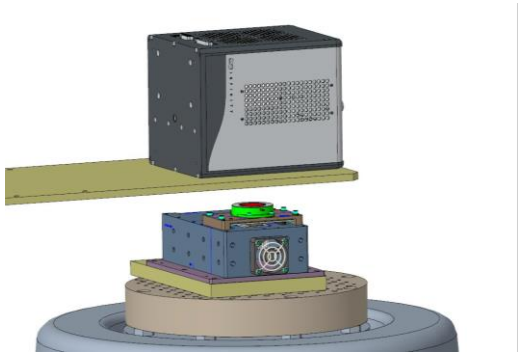

Fig. 15. Operational vibration setup

The expected operational vibration environment (including a 3-dB margin) to which the assembly is exposed is shown in Table 1. With the blackbody actively controlled to 25°C, the detector signal was acquired for

5 seconds every minute, first for a period of ~5 minutes with the shaker off, followed by alternating sequences of ~5 minutes with the shaker on, then off, then on, then off; resulting in a duration of ~25 minutes for the entire test.

Table 1. Operational vibration test levels

Frequency	Test level
20 Hz	1 X10^{-4} g^2/Hz
100 Hz	6 X10^{-4} g^2/Hz
500 Hz	6 X10^{-4} g^2/Hz
2000 Hz	1 X10^{-4} g^2/Hz
Overall	0.78 Grms

For both detectors, in all axes, the noise before, during and after vibrations did not change significantly. The noise level is similar for all tested axes. Small variations were observed on the noise level from one axis to another and are suspected to come from a drift in temperature in the bolometer field of view, mainly caused by the self-heating induced by the shaker during operation and variations in the temperature of the blackbody.

Fig. 16 shows a typical result obtained during the operational vibration tests. For each pixel, the noise was calculated over five consecutive one-second periods, and the median of the five measurements is assigned as the noise of the pixel. For each figure, the top part shows the median noise for all the native pixels (28-µm pitch) of the central area while the bottom part provides the median noise for all the detector pixels (140-µm pitch) of the same area.

It was observed that the detector pixel noise was systematically higher than what was measured in the NEP setup (c.f. section 3.3). A closer inspection of the results suggest that this is due to environmental temperature stability, mainly in the blackbody that was used as a scene during the measurements.

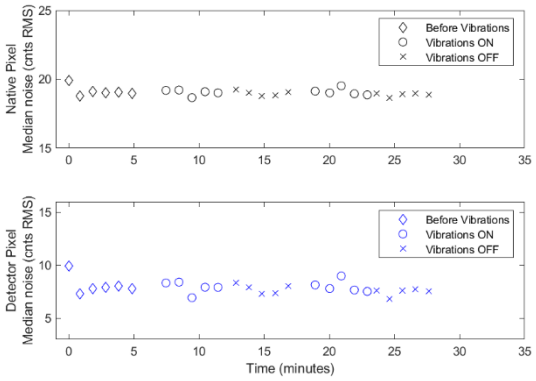

Fig. 16. Detector noise during operational vibrations

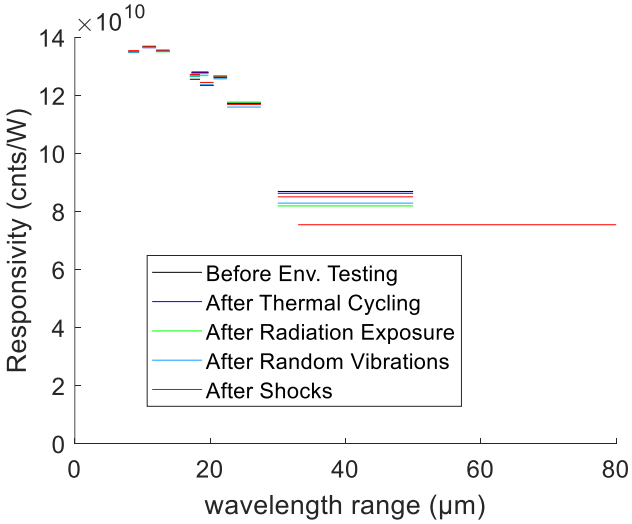

Fig. 17. Spectral responsivity of detector 2024-0009 throughout environmental test campaign

4. Conclusions

This paper presented a detector developed specifically to address broadband and far-IR applications. The FPA and detector assembly were described, including the possibility of implementing signal correction features to optimize the noise performance.

Four detector assemblies were subjected to a test campaign including functional and performance characterization as well as environmental tests. Two detectors successfully passed a flight-like qualification campaign including temperature cycling, total ionizing does exposition, random vibrations and SRS shocks. Two other detectors demonstrated their ability to be used in an airborne campaign, including operational vibrations and vacuum integrity.

The detectors performance was shown to be stable throughout survival and operational tests, and to provide for important improvements over legacy detectors. IRM1024-based detectors have already been flown in low-Earth orbit for a commercial constellation mission and are considered for institutional missions / instruments such as AOS-TICFIRE and for lunar and space exploration applications (mineralogy, cold surface temperature measurements).

Acknowledgements

This project is undertaken with the financial support of the Canadian Space Agency.

References

[1] N. E. Bowles *et al.*, The Lunar Thermal Mapper instrument for the Lunar TrailBlazer mission, 2382, 56th LPSC (2025).

[2] P. Clark *et al.*, Overview of Primitive Object Volatile Explorer (PrOVE) smallsat concept, Proc. SPIE 10769 (2018) 107690J.

[3] R. Evans *et al.*, Design and testing of the Lunar Thermal Mapper optics, Proc. SPIE 13092 (2024) 130922K.

[4] B. Fisette *et al.*, Design and fabrication of a scalable high-reliability vacuum sealed package for infrared detectors, 4th Electronics System Integration Technology Conference (2012).

[5] B. Fisette *et al.*, Novel vacuum packaged 384x288 broadband bolometer FPA with enhanced absorption in the 3-14 µm wavelength range, Proc. SPIE 10177 (2017) 101771R.

[6] F. Généreux *et al.*, Small uncooled bolometers with a broad spectral response, Proc. SPIE 10624 (2018) 106241D.

[7] F. Généreux *et al.*, Ultra-broadband uncooled infrared camera core for multi-spectral and far-infrared Earth, lunar and planetary observation, SSC24-P2-05, 38th Annual Small Satellite Conference (2024).

[8] C. I. Honniball *et al.*, Evaluating the spectroradiometric performance of an uncooled midwave infrared hyperspectral interferometer using a microbolometer array detector, Optical Enginnering 59(7) (2020) 074103.

[9] S. Ilias *et al.*, Deposition and characterization of gold black coatings for thermal detectors, Proc. SPIE 7750 (2010) 77501J.

[10] C. Proulx *et al.*, The EarthCARE broadband radiometer detectors, Proc. SPIE 7453 (2009) 74530S.

[11] C. Proulx *et al*., Design and instrumentation of an airborne far infrared radiometer for in-situ measurements of ice clouds, Proc. SPIE 9973 (2016) 99730F-1

[12] Y. Wang *et al.*, Investigation on reliability of thermoelectric cooler for space remote sensing, 2013 Internationa Conference on Quality, Reliability, Risk, Maintenance, and Safety Engineering (QR2MSE) (2013).

[13] C. L. Young *et al.*, Trutinor: a conceptual study for a next-generation Earth radiant energy instrument, Remote sens. (2020) 12, 3281.

[14] S. Zechlau *et al.*, The Earth Explorer EarthCARE is launched, APARC newsletter no. 63 (2024) 25-30.